Journal of
Materials Chemistry A

Materials for energy and sustainability

Accepted Manuscript

This article can be cited before page numbers have been issued, to do this please use: K. K. Kariattukarakaran Thilakan, S. Ghorai, W. Liu, L. Häggström, F. Lindgren, V. Pomjiakushin, P. Beran, O. Gutfleisch, P. Svedlindh and J. Cedervall, *J. Mater. Chem. A*, 2025, DOI: 10.1039/D5TA03047A.

ROYAL SOCIETY OF CHEMISTRY

rsc.li/materials-a

View Article Online
DOI: 10.1039/D5TA03047A

Journal Name

ARTICLE TYPE

Cite this: DOI: 00.0000/xxxxxxxxxx

Revealing complex magnetic interactions in Fe_2P-based compounds: A study using Mössbauer spectroscopy and neutron diffraction†

Karthika K. Thilakan,[a] Sagar Ghorai,[b] Wei Liu,[b] Lennart Häggström,[c] Fredrik Lindgren,[a] Vladimir Pomjakushin,[d] Premysl Beran,[e,f] Oliver Gutfleisch,[b] Peter Svedlindh,[g,h] and Johan Cedervall*[a]

Received Date
Accepted Date

DOI: 00.0000/xxxxxxxxxx

The magnetic properties of $Fe_{2-2x}Mn_{2x}P_{1-x}Si_x$ $(0 \leq x \leq 0.5)$ compounds are studied by neutron diffraction, Mössbauer spectroscopy, and magnetometry. DC magnetization measurements indicate that compounds with $0.2 \leq x \leq 0.5$ undergo a paramagnetic to ferromagnetic transition, with the Curie temperature increasing as x increases. In contrast, compounds with $0 < x \leq 0.15$ show unclear magnetic ordering in DC magnetization measurements, while AC magnetization measurements display frequency-dependent peaks, indicating glassy spin dynamics. For the $x = 0.125$ sample, AC magnetization measurements under applied DC fields suggest that the transition at 150 K corresponds to a complex antiferromagnetic (AFM) structure. Mössbauer spectroscopy reveals four distinct regions of hyperfine interactions for different x values, suggesting extreme sensitivity in the magnetic behaviour with Mn and Si substitutions. For $0 < x < 0.15$, a drop in the magnetic hyperfine field supports the existence of a complex AFM structure. Neutron diffraction on the $x = 0.1$ sample confirms an incommensurate AFM structure with a propagation vector $q_x = 0.2204(4)$, consistent with the Mössbauer and magnetization results.

1 Introduction

Magnetocaloric materials have attracted significant interest as a promising alternative to traditional gas compression methods for magnetic refrigeration [1–4]. Fe_2P-based compounds are among the most promising candidates for magnetic refrigeration due to their large magnetocaloric effect (MCE) resulting from the first-order magnetic transition (FOMT) [5–9]. Fe_2P and its derivatives when substituted with Mn and Si exhibit an intriguing phase diagram, Figure 1. Fe_2P and Mn_2P adopt a hexagonal $P\bar{6}2m$ structure, while the intermediate compound FeMnP crystallizes in an orthorhombic *Pnma* structure (Co_2P-type). Substituting P with Si in Fe_2P gives rise to another orthorhombic structure. However, single-phase compounds corresponding to Fe_2Si and Mn_2Si cannot be synthesized, as they are in a multiphase region. The center of this phase diagram is occupied by $FeMnP_{0.5}Si_{0.5}$, which retains the Fe_2P structure.

Fe_2P-based compounds are particularly intriguing due to their tunable transition temperature, non-toxic and non-critical raw materials, and high isothermal magnetic entropy change [10]. These compounds crystallize in a hexagonal $P\bar{6}2m$ space group with two independent metal sites; tetrahedral $3f$ and pyramidal $3g$ sites (Figure 2). Several studies have shown that Mn preferentially occupies the larger pyramidal $3g$ site in Mn-substituted compounds of Fe_2P [11–14]. The occupation of the non-metal atoms P and Si in the $1c$ and $2b$ sites shows no preference in almost all cases. However, XRD refinement and energy calculations of the compound $Fe_{0.6}Mn_{1.4}P_{0.6}Si_{0.4}$ using the Korringa-Kohn-Rostoker Coherent Potential Approximation (KKR-CPA) [15] and the neutron diffraction study of $Fe_{0.70}Mn_{1.25}P_{1-x}Si_x$ (x = 0.45, 0.50, 0.55) by Miao et al. [16] suggest that Si atoms preferentially occupy the $2c$ site. A relation between the Si content and the magnetic hyperfine field at the Fe sites in $Fe_2P_{1-x}Si_x$ compounds has been established using Mössbauer spectroscopy [17]. It was observed

[a] Department of Chemistry - Ångström Laboratory, Uppsala University, Box 538, 751 21 Uppsala, Sweden. E-mail: johan.cederall@kemi.uu.se
[b] Institute of Materials Science, Technical University of Darmstadt, 64287 Darmstadt, Germany.
[c] Department of Physics and Astronomy, Uppsala University, Box 516, 751 20 Uppsala, Sweden.
[d] Laboratory for Neutron Scattering and Imaging, Paul Scherrer Institut, 5232 Villigen, Switzerland.
[e] European Spallation Source ESS ERIC, Box 176, 221 00, Lund, Sweden.
[f] Nuclear Physics Institute, ASCR, Hlavni 130, 25068 Rez, Czech Republic.
[g] Department of Materials Science and Engineering, Uppsala University, Box 35, 751 03 Uppsala, Sweden.
[h] WISE - Wallenberg Initiative Materials Science for Sustainability, Department of Materials Science and Engineering, Uppsala University, SE-751 03 Uppsala, Sweden.
† Supplementary Information available: [details of any supplementary information available should be included here]. See DOI: 00.0000/00000000.

View Article Online
DOI: 10.1039/D5TA03047A

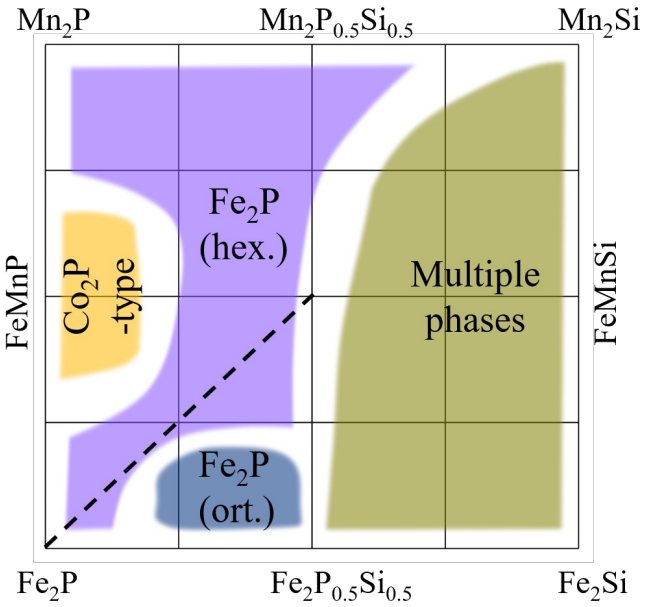

Fig. 1 Quaternary phase diagram of the Fe-Mn-P-Si system. The samples studied in this paper lie on the dotted line.

that the magnetic hyperfine field at the tetrahedral and pyramidal Fe sites increases with increasing Si content. Another significant result from Mössbauer studies[12,18] is that the magnetic Fe hyperfine field at the tetrahedral 3f site increases considerably from 11.4 T in Fe_2P to 22.8 T in $FeMnP_{0.5}Si_{0.5}$. The magnetic hyperfine field at the 3g pyramidal site cannot be measured in $FeMnP_{0.5}Si_{0.5}$ due to the absence of Fe atoms at this site. However, Fruchart et al.[15] measured the hyperfine field at the 3g site for the compound $Fe_{1.4}Mn_{0.6}P_{0.6}Si_{0.4}$ at 84 K as 19.5 T, which can be compared with 17.2 T in Fe_2P[18].

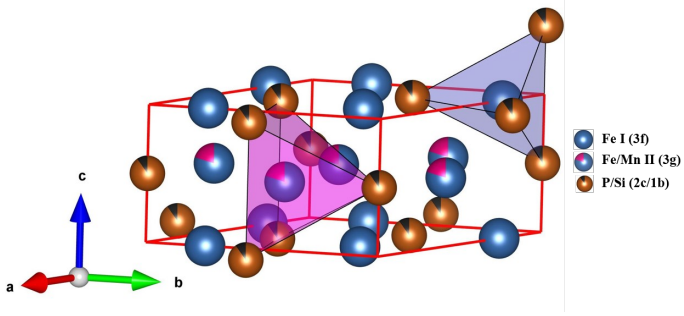

Fig. 2 Coordination polyhedra of the metal atoms: tetrahedral 3f site (represented as blue polyhedron) and pyramidal 3g site (represented as pink polyhedron).

The MCE is quantified by measuring isothermal entropy and adiabatic temperature changes in materials. Large values of these parameters indicate the strong potential of a material for magnetocaloric applications. Although a high isothermal magnetic entropy change is observed in the $(Fe,Mn)_2(P,Si)$ system, considerable thermal hysteresis (ΔT_{hys} = 35 K) is associated with FOMT[10]. The isothermal entropy change (ΔS_{mag}) of $FeMnP_{0.5}Si_{0.5}$ with an applied magnetic field of 2 T is 16.5 $Jkg^{-1}K^{-1}$, making it very competitive with other materials for magnetic cooling applicaitons[19]. Corresponding values for other magnetocaloric materials are 5.2, 18.4, 21.7 and 15 $Jkg^{-1}K^{-1}$, for Gd, $Gd_5Si_2Ge_2$, $LaFe_{11.6}Si_{1.4}$ and $Ni_{50.2}Mn_{35.0}In_{14.8}$ (Heusler), respectively[20]. The search for optimal Fe:Mn and P:Si ratios is key to obtaining reduced thermal hysteresis while maintaining the giant magnetocaloric effect in the Fe-Mn-P-Si system. So far, the studies on $(Fe,Mn)_2(P,Si)$ compounds were mainly focused on keeping equal amounts of Fe and Mn[10,12,21–23]. These compounds, which crystallize in the hexagonal Fe_2P-type phase, are explored to understand the magnetic interactions behind the physics of magnetic cooling. In Fe_2P, the magnetic moments are ferromagnetically ordered along the hexagonal c-axis below the transition temperature[7,18] T_c while in $FeMnP_{0.5}Si_{0.5}$ they are aligned along the a-axis[22]. However, $FeMnP_{0.75}Si_{0.25}$ shows a complex antiferromagnetic (AFM) ordering[21]. Therefore, it is important to investigate the compositions between Fe_2P and $FeMnP_{0.5}Si_{0.5}$ to understand the stability of the ferromagnetic state (FM) and ultimately to develop improved design guidelines for magnetocaloric materials.

In this work, a series of stoichiometric compounds $Fe_{2-2x}Mn_{2x}P_{1-x}Si_x$ ($0 \leq x \leq 0.5$) were synthesized using the drop synthesis method and studied through neutron diffraction, magnetization measurements, and Mössbauer spectroscopy.

2 Methods

2.1 Synthesis

Master alloys of Fe_2P and $FeMnP_{0.5}Si_{0.5}$ were prepared from stoichiometric amounts of iron (Leico Industries, purity 99.99+%. Surface oxides were reduced in H_2-gas.), manganese (Institute of Physics, Polish Academy of Sciences, purity 99.999%), phosphorus (Alfa Aesar, purity 99.999+%) and silicon (Highways International, purity 99.999%) using the drop synthesis method[24]. Intermediate samples of $Fe_{2-2x}Mn_{2x}P_{1-x}Si_x$ were prepared by mixing stoichiometric amounts of the master alloys. All samples were sealed in evacuated silica ampules and annealed at 1370 K for 2 h, followed by heat treatment at 1270 K for 10 days and rapid quenching.

2.2 Diffraction

X-ray diffraction experiments were performed using a Bruker D8 Advance operating with CuKα radiation and equipped with a LynxeyeXE position sensitive detector. Neutron powder diffraction (NPD) was employed using the HRPT instrument[25] at SINQ (PSI, Villigen Switzerland). A Ge monochromator (reflection 400) was used that gives a wavelength of 2.45 Å. All samples were measured in a temperature range of 10 to 300 K.

The obtained diffraction data was analyzed using the Rietveld method[26] implemented in FullProf software[27]. In the refinements, several structure parameters, including atomic positions, occupancies, and displacement, were allowed to vary. For incommensurate magnetic structures, the magnetic propagation vectors, **k**, were investigated using **k**-search implemented in the FullProf Suite. The obtained **k**-vectors were used as input parameter to find irreducible representations (IR) with the SARAh software[28]. The obtained IRs were later implemented in full-pattern

View Article Online
DOI: 10.1039/D5TA03047A

magnetic structure refinements.

2.3 Magnetometry

A Quantum Design magnetic property measurement system was used to assess the magnetic properties of samples. The temperature dependent magnetization under field-cooled cooling (FC) and field-cooled warming (FCW) conditions was measured using an applied magnetic field of $\mu_0 H = 10$ mT. Temperature- and frequency-dependent AC susceptibility measurements were performed to study the low-frequency relaxation behavior of the compounds with $0.05 \leq x \leq 0.15$ using an AC magnetic field amplitude of $\mu_0 H_{AC} = 0.4$ mT.

2.4 Mössbauer Spectroscopy

Mössbauer measurements were carried out on a spectrometer working with a constant acceleration type of vibrator and a ^{57}CoRh source. The spectra were recorded at low temperatures in an Oxford He-flow cryostat and at high temperatures in a Ricor furnace, respectively. The $Fe_{2-2x}Mn_{2x}P_{1-x}Si_x$-samples were mixed with inert BN and enclosed in sealed kapton pockets. The absorbers formed thus had a sample concentration of ~2-20 mg/cm^2. Calibration spectra were recorded at 295 K using natural Fe metal foil as a reference absorber. The spectra were folded and fitted using the least square Mössbauer fitting program Recoil to obtain the values of the center shift (CS) versus natural α-Fe at 295 K, the electric quadrupole splitting (QS) (in the paramagnetic regime), the electric quadrupole shift (ε) and the magnetic hyperfine field (B_{hf}) (in the magnetic regime), the full-width at half maxima (W) of the Lorentzian absorption lines and the spectral areas (A).

3 Results

3.1 Phase analysis

All samples are of high purity, with only trace amounts of secondary phases, as shown in Figure 3 for $x = 0.1$. Structural refinements show that all samples crystallize in the Fe_2P-type structure, space group (SG) $P\bar{6}2m$. The evolution of the unit cell parameter, studied using XRD, Figure S1 in SI (Supplementary Information), gives a clear trend where a (c) increases (decreases) with increasing amount of x. This also affects the c/a-ratio, which decreases with increasing level of substitution. There is a shift in the unit cell parameters between x = 0.25 and 0.375 due to magnetostriction as samples with x > 0.25 have T_C above RT. The unit cell parameters for the master alloys (Fe_2P and $FeMnP_{0.5}Si_{0.5}$) are in excellent agreement with the values previously reported, which in combination with the NPD results indicate that the substitutions have been successful. The structure refinement to the NPD data confirms that Mn preferably occupies the pyramidal 3g position even in low concentrations, shown as an inset in Figure 3, in agreement with previous findings[16,21,22,29]. Varying the Fe and Mn occupancies were tested in the refinements, but as it did not improve the refined model they were left in their nominal compositions.

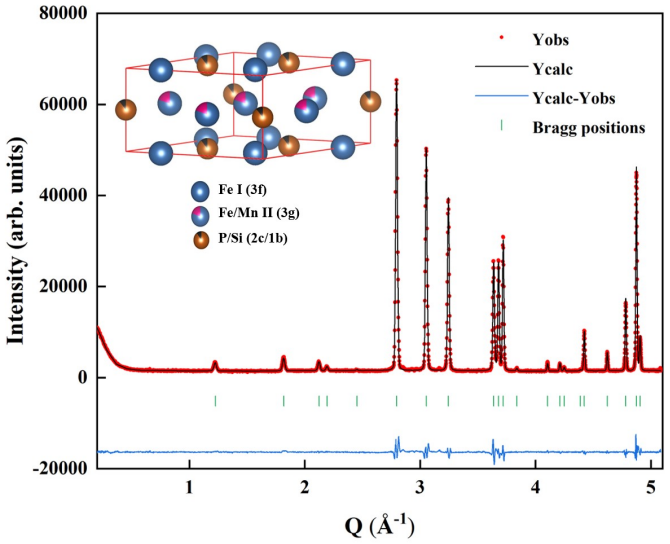

Fig. 3 Neutron diffraction (λ = 2.45 Å) pattern for $Fe_{1.8}Mn_{0.2}P_{0.9}Si_{0.1}$ at room temperature. The refined structure model is shown as an inset.

3.2 Mössbauer Spectroscopy

3.2.1 Paramagnetic regime

In Figure 4 the Mössbauer spectra in the paramagnetic regime are presented along with the spectral areas for the two crystallographic sites. The area of Fe(2) at pyramidal 3g sites decreases with increasing x and at $x = 0.5$, ($FeMnP_{0.5}Si_{0.5}$), all contributions to the pattern come from Fe(1) at tetrahedral 3f sites. This confirms the findings from NPD that Mn atoms are solely located at the pyramidal 3g site all through the substitution series. The fitted results using one Mössbauer pattern each for Fe(1) and Fe(2) are presented in Table S1.

A detailed study of the Fe(1) subspectrum for $x = 0.5$ and $x = 0.375$ shows some asymmetric doublet behavior that is caused by an atomic disorder in the near surroundings of Fe(1) at the tetrahedral 3f site. It is expected since the four nearest neighbour (nn) atoms P or Si can vary. The nn to the 3f site is 2 P or Si atoms at the 1b site and 2 P or Si atoms at the 2c site. Each surrounding would give slightly different Mössbauer subspectra, which may explain the asymmetry and broadening in the spectrum as shown in Figure 4. It has been argued that Si preferentially occupies the 2c-site[15], however, by analysing the Mössbauer hyperfine spectra of $Fe_2P_{1-x}S_x$ with $0.10 \leq x \leq 0.16$ the P/Si substitution is shown to be almost random[17]. However, the resolution in the present spectra in the paramagnetic regime is too low to resolve any preference of the P/Si occupation.

3.2.2 Magnetic regime

The hyperfine parameters are affected differently due to the various amounts of P, Si, Mn and Fe atoms around each Fe metallic site. The spectra have therefore been fitted with 2 to 4 sextet patterns depending on the x-value (Figure 5). In the fitting, all subspectra representing Fe at the 3f site have the constraint of having the same central shift CS. Similar constraints have also been used for Fe at the 3g site. These constraints were used pri-

View Article Online
DOI: 10.1039/D5TA03047A

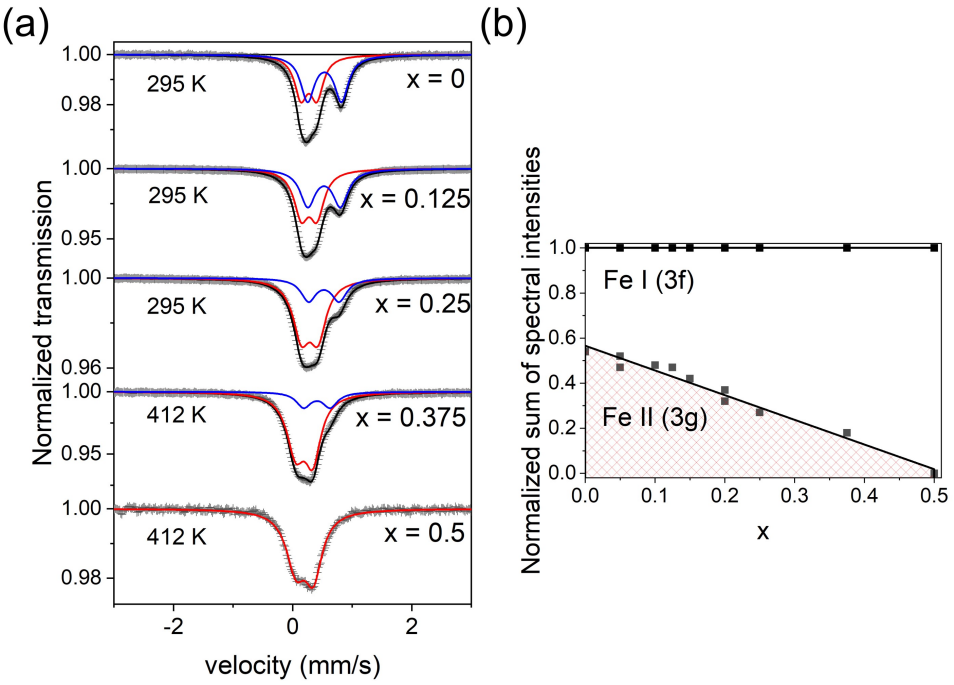

Fig. 4 a) Mössbauer spectra in the paramagnetic regime for different values of x. The red and blue subspectra emanate from Fe(1) at the tetrahedral $3f$ and Fe(2) at the pyramidal $3g$ positions, respectively. b) Normalized sum of spectral intensities of tetrahedral Fe(1) and pyramidal Fe(2) versus x in $Fe_{2-2x}Mn_{2x}P_{1-x}Si_x$.

marily to minimize the number of fit variables. The variation of the *CS* values for different surroundings was furthermore found to be small in the spectrum in the paramagnetic regime for Fe both at $3f$ and $3g$, justifying the constraints used. The average hyperfine results from the fitting of spectra at 85 K are presented in Figure 6 and Table S2.

In order to find the polar (θ) and azimuthal (ϕ) angles of the magnetic fields versus the principal axes of the electric field gradient (EFG) tensor at 85 K the factor $K = \frac{2\varepsilon}{QS}$ connecting the two electric quadrupole parameters QS and ε can be calculated using the expression:

$$K = \frac{3\cos^2\theta - 1 + \eta\sin^2\theta\cos 2\phi}{2\sqrt{1+\frac{\eta^2}{3}}} \quad (1)$$

where η is the EFG asymmetry parameter and the angles θ and ϕ refer to the situation at 85 K. Given the magnetic state of the compounds at 85 K, QS cannot be directly measured. However, using previously reported values for Fe_2P[30], $QS(295\text{ K})/QS(85\text{ K}) \approx 1.15$ for both Fe sites. Therefore, the values of K in Figure 6 (d) has been calculated as $K \approx 1.15\frac{2\varepsilon(85K)}{QS(295K)}$. The principal z axis of the EFG has been found to be in the ab plane and also a negative sign for QS for both Fe sites in Fe_2P[31]. The calculated values of K show four different regions: *i*) $K \sim -0.5$ for x close to 0, *ii*) $K \sim 0$ for $x \sim 0.1$, *iii*) $K \sim -0.9$ for $x \sim 0.25$ and *iv*) $K \sim 0.9$ for $x \sim 0.4-0.5$ (Figure 6(d)) .

Region *i* represents the ferromagnetic structure with the magnetic moments along the *c*-axis. The polar angle is 90° with a small asymmetry parameter η, K would theoretically be –0.5 as also found experimentally here. With only a slight amount of Mn and Si substitution, B_{hf} drops at both crystal sites and the electric quadrupole ratio drops to zero, making the system enter region *ii*.

Region *iv* represents the ferromagnetic structure with the magnetic moments along the *a*-axis. Since the orientation of the *z*-axis of the electric field gradient tensor is in the *ab*-plane, the polar angle will be unknown, as will the azimuthal angle for Fe at the tetrahedral $3f$ site. Experimentally $K \sim 0.9$ is observed, which can be interpreted as having the *z*-axis along the *a*-axis with small contributions from the asymmetry parameter (Eq. (1)).

Regions *ii* and *iii* are more difficult to interpret from the experimental values of K. The resonance lines are broad due to the different possible *nn* configurations of the Fe atoms. The K-value has therefore to be interpreted as a value averaged over all possible *nn* configurations. In region *ii* the average value for K is close to 0 which may be interpreted as a region with varying polar and azimuthal values, a possible antiferromagnetic helical structure for the magnetic moments. The drop in the magnetic hyperfine field in region *ii* is further an indication of a more complex antiferromagnetic structure. Judging from the B_{hf} results, region *iii* seems to be dominantly ferromagnetic in character.

3.2.3 Mössbauer temperature study of the antiferromagnetic region *ii*

Here we present a temperature study of the sample with $x = 0.125$ as a representative for the antiferromagnetic region *ii*. The Mössbauer spectra above 177 K could be identified as emanating from a paramagnetic phase, while spectra below 152 K were emanating from a phase where magnetic fields were acting

View Article Online
DOI: 10.1039/D5TA03047A

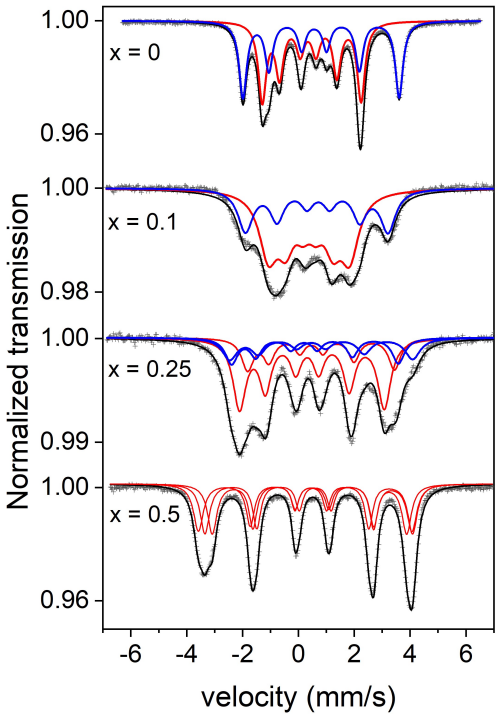

Fig. 5 Mössbauer spectra of $Fe_{2-2x}Mn_{2x}P_{1-x}Si_x$ at 85 K. Blue and red represent Fe at the pyramidal ($3g$) and tetrahedral ($3f$) sites, respectively.

on the Fe nucleus (Figure 7).

The spectra in the paramagnetic regime were fitted using two doublets. In the magnetically ordered state, the spectra exhibited significant broadening due to variations in the local environment, where different numbers of neighboring Mn and P/Si atoms influence the magnetic field at the Fe nucleus. This broadening was approximated by four sextets, two representing Fe at the $3g$ site and two at the $3f$ site. Table S3 presents the fitted results, while Figure 7 displays representative spectra.

It is evident that no Fe magnetic moment ordering exists above 150 K for the samples within the time scale of the Mössbauer transition $\sim 10^{-7}$ s and longer. However, the AC susceptibility results indicate slow spin dynamics with glassy behavior at ~200 K and 320 K (cf. Figure 9 below); the frequency range $1.7 - 170$ Hz corresponds to a time scale range of $1 - 100$ ms. The absence of a magnetic hyperfine splitting of the ^{57}Fe Mössbauer spectrum at temperatures $T > 150$ K can have at least two explanations. One explanation could be that the slow spin dynamics detected in the AC susceptibility measurement originate solely from the Mn magnetic moments. Another relating explanation is that the local Fe magnetic moment disappears at temperatures above the antiferromagnetic ordering temperature. The latter explanation connects to the rare case of mixed magnetism, i.e. the coexistence of strong and weak magnetism, discussed for hexagonal FeMn(P,Si) [5].

The AC susceptibility and Mössbauer results are consistent with the onset of magnetic ordering at ~150 K. The observed values of ε (~0.00 mm/s) are significantly lower compared to QS (~-0.36 mm/s and -0.56 mm/s for Fe at the $3f$ and $3g$ sites, respectively). This suggests that a magnetic structure with moments aligned along the c-axis can be ruled out, as such an arrangement would yield an electric quadrupole ratio $K = \frac{2\varepsilon}{QS}$ of -0.5 (see the section on the magnetic regime above).

3.3 Magnetic characterisation

The temperature-dependent magnetization of the compounds studied is shown in Figure 8 (a, b). Fe_2P ($x = 0$) shows a paramagnetic (PM) to ferromagnetic (FM) phase transition with a $T_C = 216(2)$ K, similar to the previously reported value [30]. A phase transition from PM to FM is also observed in the samples with $0.2 \leq x \leq 0.5$. For these four compounds, T_C increases with increasing x, although the increase in T_C levels off at higher x values. Magnetic transition temperatures of Fe_2P-type compounds are often related to the atomic distances between the magnetic atoms situated in the $3f$ and $3g$ sites. The positions of the $3f$ and $3g$ sites and their shortest interatomic distances (d_{3f-3g}) were extracted from the neutron diffraction refinements. The values of d_{3f-3g} and T_C are shown in Table 1. It is clear that an increase of d_{3f-3g} follows with an increase in T_C for the four compounds with $0.2 \leq x \leq 0.5$. In Fe_2P, both the $3f$ and $3g$ sites are occupied by Fe, which is unlikely for the rest of the compounds. Interestingly, these four compounds exhibit thermal hysteresis (ΔT_{hys}), i.e. a difference in the magnetic phase transition temperature between the FC and FCW magnetization curves. The presence of ΔT_{hys} is often used as an indication of a FOMT [19].

Table 1 Values of T_C, inter-atomic distances d_{3f-3g}, and temperature hysteresis ΔT_{hys} of the compounds with $0.2 \leq x \leq 0.5$. The values of T_C are taken from the FC magnetization versus temperature curves at $\mu_0 H$ = 0.01 T.

x	T_C^{FC} (K)	d_{3f-3g} (Å)	ΔT_{hys} (K)
0	216	2.6272(4)	20
0.2	196	2.6225(7)	20
0.25	266	2.6523(5)	18
0.375	362	2.6551(6)	10
0.5	380	2.6678(4)	14

The compounds with $0 < x \leq 0.15$ exhibit a much lower magnetization with unclear magnetic ordering (cf. Figure 8(b)). The temperature-dependent magnetization curves resemble those of materials with glassy behavior. To investigate this behavior further, temperature- and frequency-dependent AC magnetic susceptibility measurements have been performed for the $x = 0.125$ compound; the results are shown in Figure 9. The real component of the AC-susceptibility (cf. Figure 9(a)) exhibits a clear frequency dependence at temperatures above 150 K. The imaginary component reveals several loss peaks (Figure 9(b)). The presence of several frequency-dependent loss peaks is indicative of different contributions to magnetic dissipation in the temperature range of $150 \text{ K} < T < 400$ K. From a comparison of the AC susceptibility and Mössbauer results, it is concluded that the slow spin dynamics in this temperature range is solely due to the Mn magnetic moments. At the same time, the disappearance of dissipation at $T < 150$ K is in accordance with the order of AFM at low tem-

View Article Online
DOI: 10.1039/D5TA03047A

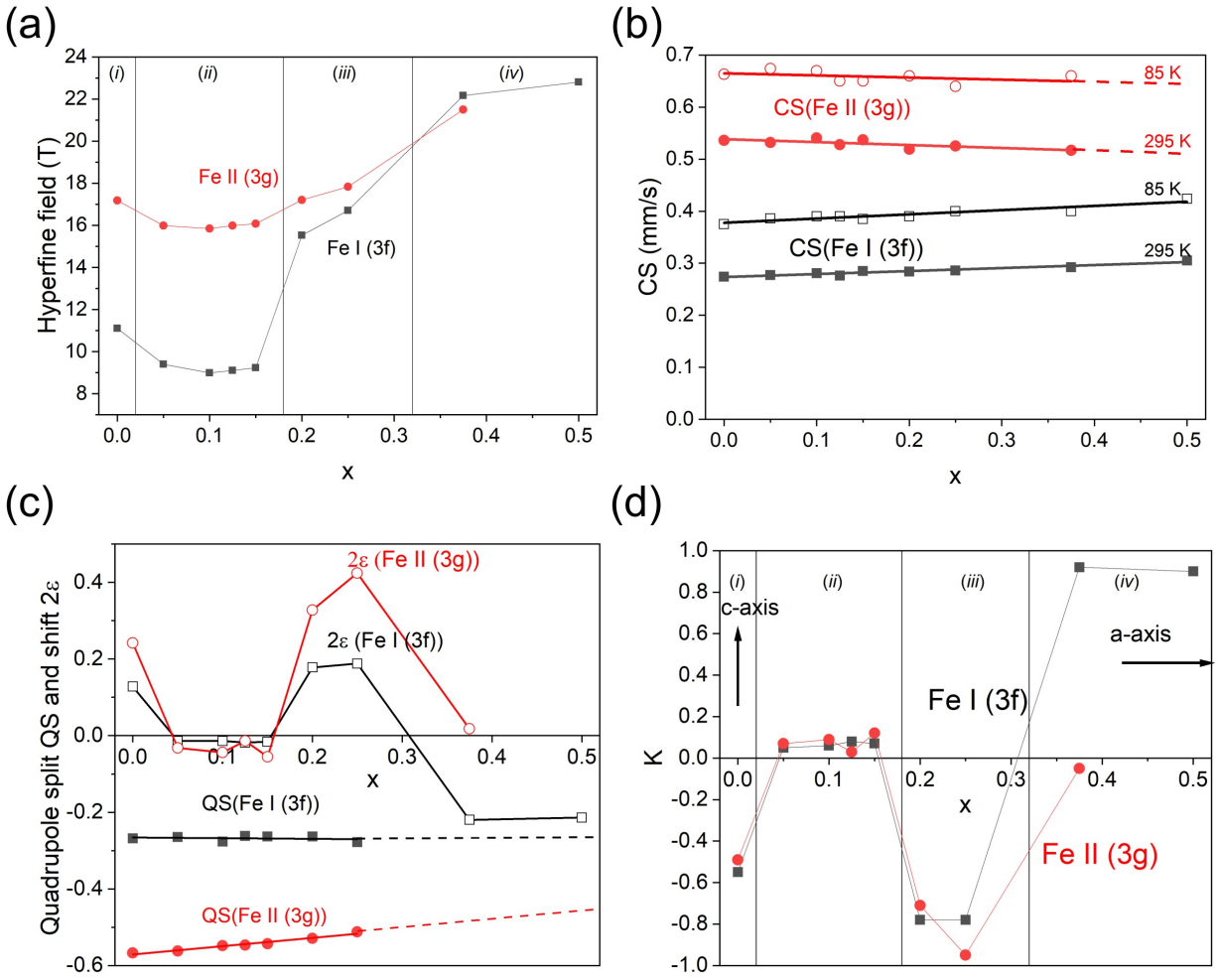

Fig. 6 a) The average magnetic fields at 85 K for Fe at the tetrahedral $3f$ site and pyramidal $3g$. b) The center shift CS versus natural α-Fe at 295 K for Fe_{3f} and Fe_{3g} at 295 K and 85 K. c) The electric quadrupole splitting QS at 295 K and electric quadrupole shift 2ε at 85 K in mm/s. d) The electric quadrupole ratio $K = \frac{2\varepsilon}{QS}$ at 85 K.

perature involving both local Fe and Mn moments, which will be discussed below when describing the results of the magnetic structure analysis.

In order to get more insight into the glassy spin dynamics, Figure 9 (c) and (d) show AC susceptibility versus temperature results for fixed AC frequency (1.7 Hz and 170 Hz) along with superimposed DC magnetic fields (0 - 5 mT). The real component of the AC-susceptibility (cf. Figure 9(c)), including its frequency dependence is suppressed by the superimposed DC magnetic field. Even more noticeable is the suppression of the imaginary component of the AC susceptibility at $T > 150$ K. In the presence of the 1 mT DC field, the loss peak at $T \approx 320$ K vanishes, while the loss peak at $T \approx 200$ K is much reduced (cf. Figure 9 (b)). Both loss peaks vanish in the presence of 5 mT DC field, while the relaxation behavior at $T < 150$ is unaffected by the superimposed DC magnetic fields (cf. Figure 9(b)). From this it can be concluded that the spin dynamics of the antiferromagnetically ordered phase is not affected by the superimposed DC magnetic field, while the time scales of the glassy spin dynamics at $T > 150$ K are strongly DC magnetic field dependent with a shortening of the time scales with increasing DC magnetic field. A similar frequency dependent behaviour has been observed for the $x = 0.05$, 0.1, and 0.15 compounds which are discussed in the Supplementary Information.

To estimate the effective paramagnetic moment of the compounds (x = 0, 0.2, and 0.25) which show a clear PM-FM transition below 400 K, the temperature dependent inverse DC-susceptibility has been fitted to the Curie-Weiss (CW) law (Figure S3 (a) in SI)[32]. The calculated effective moments are 5.96 μ_B, 9.9 μ_B, and 10.4 μ_B per formula unit for the x = 0, 0.2, and 0.25 samples, respectively. The extracted values for the x = 0.2, and 0.25 samples are likely overestimated, since the x = 0.2 sample exhibits a Griffiths phase like behaviour[33,34] and x = 0.25 is not completely paramagnetic even at 400 K (Figure S3 (b)). Moreover, the field dependent magnetization at 400 K indicate that the samples which did not show a clear PM-FM transition (e.g. x = = 0.1 and 0.125) are also not completely paramagnetic at 400 K, as indicated in Figure S3 (b) revealing a non-linear magnetic field dependence at low fields. Therefore, among the studied compounds, in the measured temperature range, the CW law is only valid for the x = = 0 sample, yielding a calculated effec-

View Article Online
DOI: 10.1039/D5TA03047A

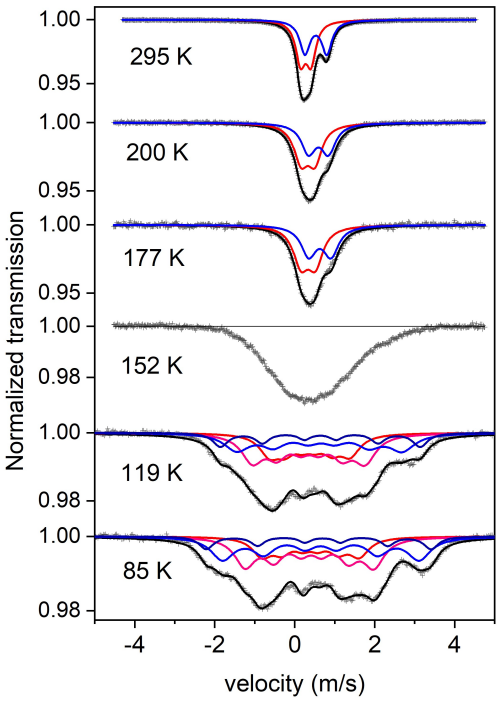

Fig. 7 Representative Mössbauer spectra of $Fe_{2-2x}Mn_{2x}P_{1-x}Si_x$ with x = 0.125. Blue subpatterns represent Fe at the pyramidal $3g$ site and red subpatterns represent Fe at the tetrahedral $3f$ site. A magnetic transition takes place between 152 K and 177 K.

tive moment of 5.96 μ_B/f.u. and a Weiss temperature of 278.3 K.

3.4 Neutron diffraction results

$Fe_{2-2x}Mn_{2x}P_{1-x}Si_x$ (x = 0.1 and 0.125) samples were examined using NPD measurements at various temperatures ranging from 300 K to 10 K. The nuclear structure was determined at room temperature (300 K), while the magnetic structure was determined at 10 K. The x = 0.125 sample has a small amount (0.7(2)%) of the secondary phase Fe_3Si. The magnetic propagation vector was determined using the **k**-search program in the FullProf software. Several possible propagation vectors were obtained from the **k**-search, which were then tested to find the propagation vector that best describes the structure.

Magnetic structures for the samples x = 0.1 and 0.125 were determined using simulated annealing and representation analysis (SARAh). Magnetic structure refinement was performed in FullProf, utilizing the basis vectors from SARAh. The neutron diffraction patterns acquired below 150 K reveal a prominent magnetic peak, 000 ± k, for both samples, indicating an incommensurate antiferromagnetic (AFM) structure with a non-zero propagation vector. Some weak satellite peaks were also observed in the Q range of 1.7-2.3 $Å^{-1}$. With the proposed **k**-vector, three magnetic models — moments aligned along the b-axis, c-axis, and in the ab-plane — were found to best fit the observed data. The primary distinction between these models lies in their fit to the weak satellite peaks, 001 ± k and 101 ± k. Figure 10 (a) presents the observed and calculated NPD patterns for the model with moments aligned along the b-axis at 10 K for x = 0.1. The magnetic contributions of the three models, along with the total calculated intensity (nuclear and magnetic contributions) for the b-axis model, are shown in Figure 10 (b), here shown for x = 0.1. The comparison reveals that the models with moments along ab and b fit the 001 ± k peak more accurately than the c-axis model, while the c-axis model fails to produce any intensity at the 101 ± k peak position. Since the model with moments along the a-axis (not shown here) does not provide a good fit to the observed NPD pattern, it suggests that the magnetic moments are more likely to align along the b-axis rather than within the ab-plane. The x = 0.125 sample shows the same behavior in the NPD patterns.

For the refinement of the nuclear structure at 300 K, several profile parameters, atom occupancy, and atomic displacement parameters were refined. Fe atoms were found to occupy only the tetrahedral $3f$ site, while the pyramidal $3g$ site is occupied by the Fe and Mn atoms. These occupancies were initially refined and subsequently fixed in the final refinement. In the magnetic structure refinement at 10 K, the same parameters as those used in the 300 K refinement were refined, with atomic occupancies fixed. A symmetric Gaussian size broadening was used to fit the magnetic reflections at low temperature. Furthermore, the magnetic moment parameters and the propagation vector were refined. Table 2 shows the results of the NPD refinement at 300 K and 10 K for the x = 0.1 sample. The unit cell parameters at 10 K; a = 5.8996(1) Å and c = 3.4507(1) Å are slightly smaller than lattice parameters at 300 K; a = 5.9156(1) Å and c = 3.4553(1) Å. The parameter a decreases continuously with decreasing temperature, while c initially decreases until 150 K, after which it starts to increase down to 10 K (Figure S4). The magnetic ordering becomes antiferromagnetic in this case, likely due to the increase in the c/a ratio below 150 K.

Figure 12 shows the proposed magnetic structure model for the x = 0.1 sample. The magnetic moments propagate sinusoidally along the a-axis with an incommensurate propagation vector of k_x = 0.2204(4). The moments of atoms at the $3f$ and $3g$ sites are aligned along the b-axis. The magnetic moments of Fe(1) and Fe/Mn(2) atoms are 0.7(2) μ_b and 2.3(2) μ_b respectively, at 10 K. From Mössbauer spectroscopy, a sinusoidal model would give broader Mössbauer spectra due to magnetic fields ranging over a wider interval, which is not directly observed here; however the suggested model is the best from the neutron diffraction analysis.

Previous studies have shown that Fe moments at $3f$ sites typically have lower magnetic moments than Mn at $3g$ sites[21,35,36]. As the temperature decreases, k_x increases for both samples (x = 0.1 and 0.125), with the x = 0.125 sample showing a larger k_x (0.2254(5)) than the x = 0.1 sample at the same temperature (Figure S5). The magnetic moments at the $3f$ and $3g$ sites also increase upon cooling, with the $3g$ site showing a slightly larger increase than the $3f$ site, here shown for x = 0.1 sample. The unusual peak shape observed for the 000 ± k in the NPD pattern could be attributed to a disorder in the magnetic arrangement or multiple propagation vectors within the magnetic structure.

View Article Online
DOI: 10.1039/D5TA03047A

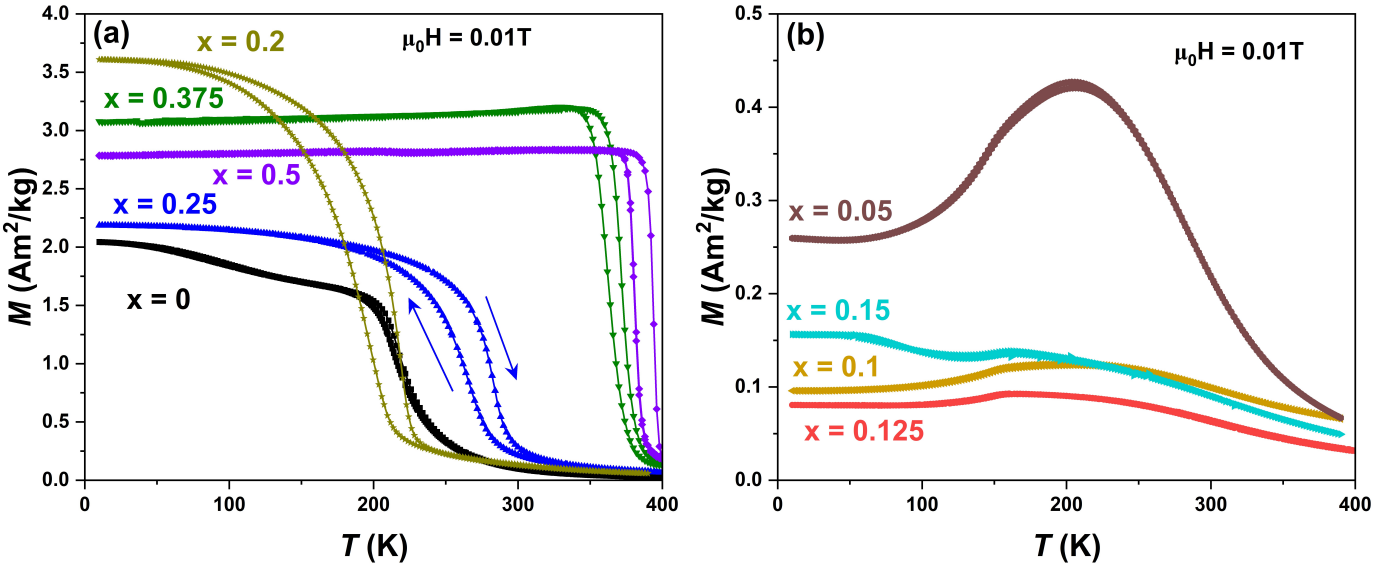

Fig. 8 Temperature dependent (a), (b) magnetization measured under FC and FCW conditions. The direction of temperature change is indicated by arrows. To clearly distinguish the temperature dependent magnetization two different scales for the magnetization are used in (a) and (b).

Table 2 Atomic coordinates, atomic displacement parameters and occupancy of Fe, Mn, P and Si atoms at 300 K and 10 K (antiferromagnetic state) obtained from refinements of neutron powder diffraction data for the sample $x = 0.1$. The full coordinates of the atomic sites are $3f$: (x 0 0), $3g$: (x 0 ½), $2c$: (⅓ ⅔ 0), $1b$: (0 0 ½). For 300 K refinement, $R_{Bragg} = 2.57$, $R_{wp} = 6.58$, $R_p = 4.49$, $\chi^2 = 6.30$. For 10 K refinement, Prop. vector $q_x = 0.2204(4)$, $R_{Bragg} = 2.51$, $R_{mag} = 3.39$, $R_{wp} = 6.71$, $R_p = 4.33$, $\chi^2 = 17.2$

		300 K			10 K			
Atom	Site	x	B_{iso} (Å)	Occ	x	B_{iso} (Å)	Occ	M (μ_b)
FeI	$3f$	0.25601(9)	0.43(2)	1	0.2559(1)	0.20(3)	1	0.7(2)
FeII/MnII	$3g$	0.5935(1)	0.43(2)	0.8/0.2	0.5923(2)	0.20(3)	0.8/0.2	2.3(2)
PI/SiI	$2c$	⅓	0.80(4)	0.9/0.1	⅓	0.79(6)	0.9/0.1	-
PII/SiII	$1b$	0	0.80(4)	0.9/0.1	0	0.79(6)	0.9/0.1	-

However, incorporating additional **k**-vectors did not result in significant changes to the magnetic structure. The temperature-dependent magnetization curve for the compounds $0 < x \leq 0.15$ from magnetometry suggests that the samples are not in a purely paramagnetic state even at 300 K. The AC susceptibility measurements for the $x = 0.125$ sample reveal a glassy spin dynamics at $T > 150$ K and a possible AFM transition below 150 K. This can be correlated to the observation of a hump with slight intensity above 150 K for the 000 ± k peak in the NPD data (Figure 11) shown here for x = 0.1 sample, indicating short-range or fluctuating magnetic correlations which has been observed before in Fe-Mn-P-Si system[37]. With decreasing temperature, this feature evolves into a slightly broadened antiferromagnetic peak at 10 K, indicating that the system is moving from short-range to long-range order with decreasing temperature, which is not unusual[38].

The broadness of the 000 ± k peak below 150 K in the NPD pattern likely arises from the system not attaining infinite magnetic correlation even at low temperatures. It is interesting to observe that a slight substitution of Mn at one of the Fe sites alters the magnetic structure, leading to moments aligning along the *b*-axis from the c-axis alignment in Fe_2P. However, more precise information on the nature of the magnetic correlations would require a polarized neutron scattering study.

An incommensurate AFM ordering has previously been reported for the $(FeMn)_2(PSi)$ system with the composition $FeMnP_{0.75}Si_{0.25}$[21]. For this composition, Fe moments align along the *a*-axis, while Mn moments align along the *b*-axis. In Fe_2P-based compounds, the chemical disorder of the 3f and 3g sites and the lattice parameter ratio c/a play a crucial role in determining the ground-state magnetic order[39].

Conclusions

The magnetic behaviour for substitutions in Fe_2P has been demonstrated with neutron diffraction, Mössbauer spectroscopy and magnetometry. It is shown that Fe_2P is extremely sensitive to distortions of the structure, here exemplified by substitutions.

From Mössbauer spectroscopy, a significant drop in the magnetic hyperfine field for $0.05 < x < 0.15$ as compared to $x = 0$ is observed. The drop in hyperfine field comes from the change of the magnetic structure, from ferromagnetic along the *c*-axis for Fe_2P, to an incommensurate antiferromagnetic structure. The magnetic hyperfine field at the tetrahedral $3f$ site has been found to increase by a factor of ~ 2 between $x = 0$ and $x = 0.5$. In fact, the Fe magnetic field at the tetrahedral $3f$ site is, at $x = 0.375$, larger than the Fe field at the pyramidal $3g$ site. This is in contrast to the situation in pure Fe_2P. These changes in the hyperfine field have a counterpart in the magnetic moments. Further Mössbauer studies are needed on samples with x closer to 0 to reveal the ex-

View Article Online
DOI: 10.1039/D5TA03047A

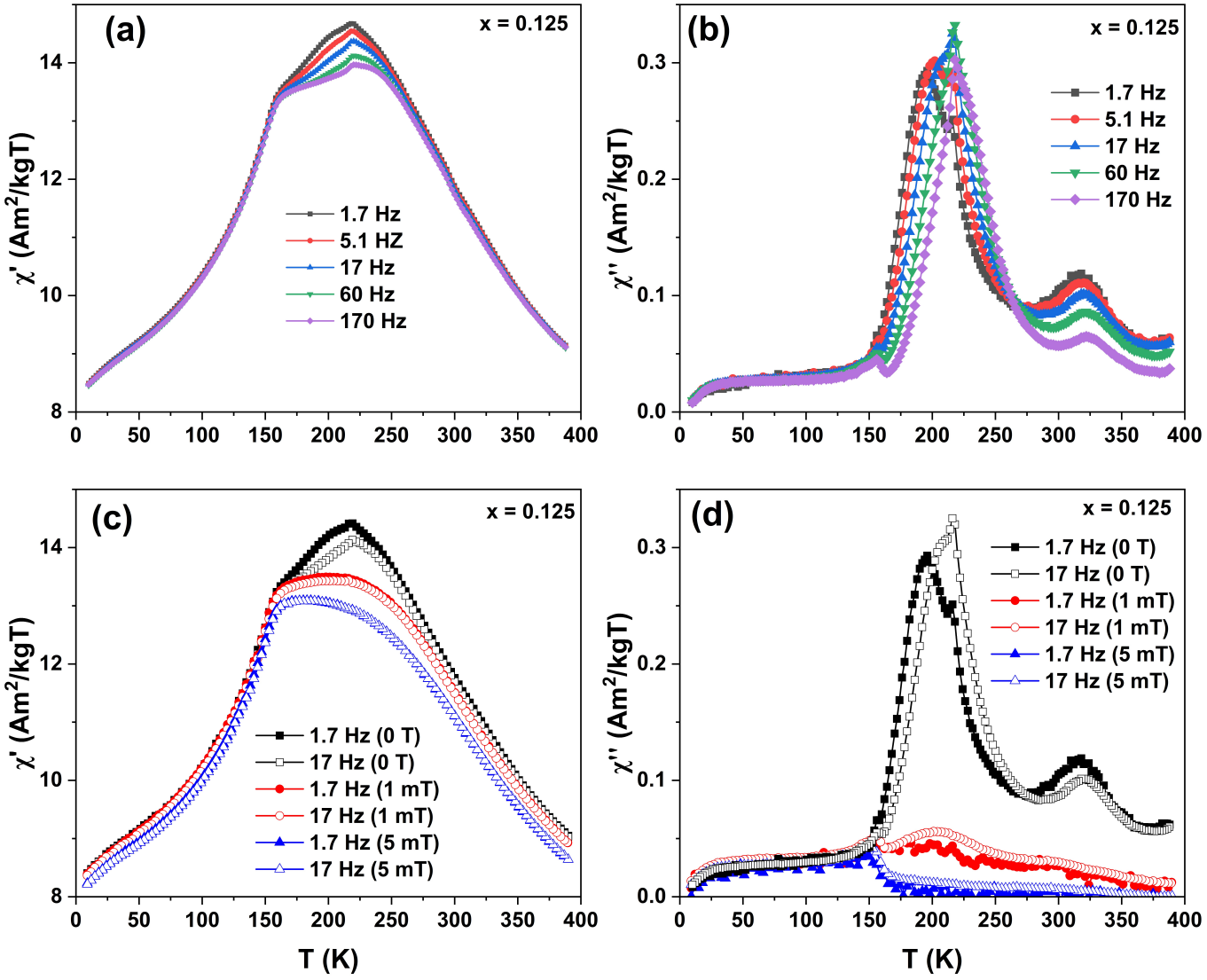

Fig. 9 Frequency and temperature dependent real and imaginary components of the AC magnetic susceptibility without applied fields (a), (b), and with superimposed DC applied fields (c), (d) respectively, for the $x = 0.125$ compound.

act nature of the antiferromagnetic structure adopted in region *ii*. From magnetometry, it is observed that the samples with a small percent Mn substitution ($0.05 < x < 0.15$) exhibit glassy spin dynamics in the temperature range 150 K $< T <$ 400 K, which arises solely from the Mn moments. The AC susceptibility with superimposed DC fields for a sample in this region, $x = 0.125$, suggests an AFM behavior below 150 K. Samples with a higher substitution for Mn ($0.2 < x < 0.5$) exhibit a PM-FM transition in DC susceptibility, the same as observed for Fe_2P. The implication of a complex AFM structure from Mössbauer spectroscopy and magnetometry is confirmed by NPD measurements for $x = 0.1$ and 0.125 samples revealing an incommensurate AFM structure with propagation vectors $k_x = 0.2204(4)$ and $0.2254(5)$ respectively at 10 K. The AFM $000 \pm k$ peak for both samples exhibits a slight intensity above 150 K, suggesting the presence of short-range magnetic correlations. Furthermore, the magnetic diffraction peaks are broader than the nuclear peaks below 150 K, indicating that the system does not attain infinite antiferromagnetic correlation even at lower temperatures.

To conclude, the effect on simultaneous substitutions of Mn and Si in Fe_2P to $Fe_{2-2x}Mn_{2x}P_{1-x}Si_x$ have been investigated with regard to their magnetic properties. The system show mainly ferromagnetic features with magnetic transition temperatures correlated to the interatomic distances between the two iron sites in the structure. However, a region $0.05 \leq x < 0.2$ have been found to have antiferromagnetic behavior, originating from an incommensurate magnetic structure propagating along the crystallographic *a*-axis with a propagation vector $k_x = 0.2204(4)$.

CRediT author contribution statement

Karthika K. Thilakan: Conceptualization, Data curation, Formal analysis, Investigation, Methodology, Visualization, Writing - original draft **Sagar Ghorai**: Data curation, Formal analysis, Investigation, Methodology, Visualization, Writing - original draft **Wei**

View Article Online
DOI: 10.1039/D5TA03047A

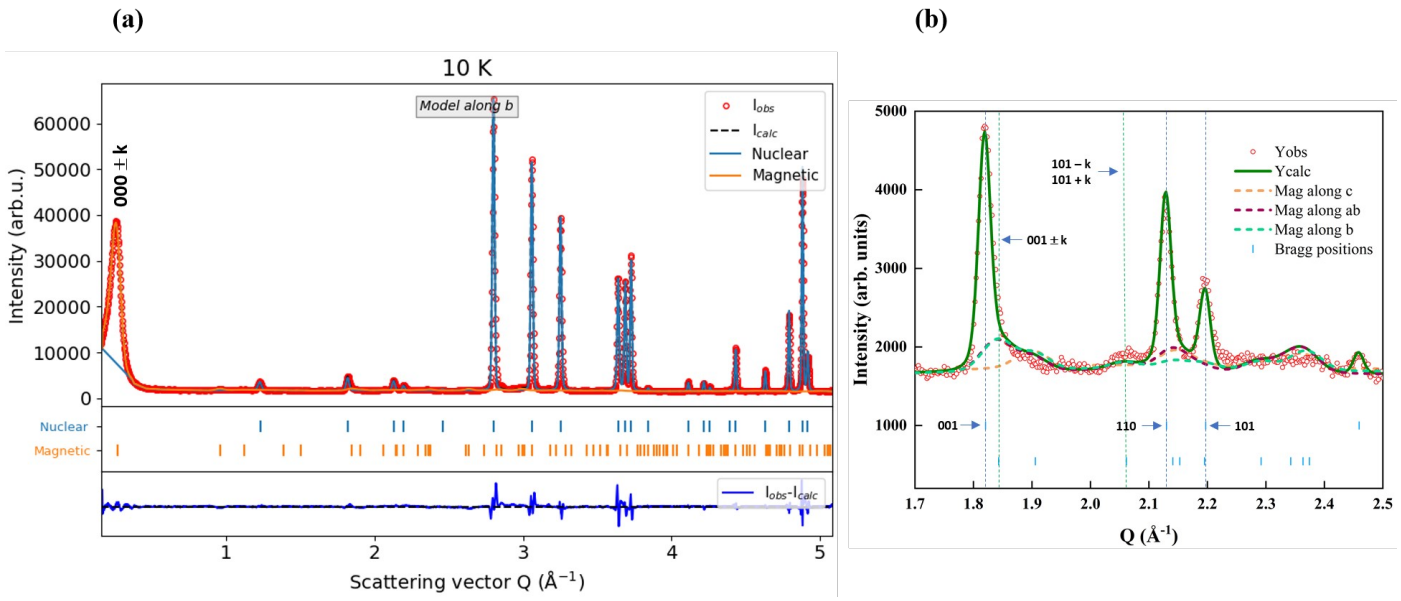

Fig. 10 (a) Observed and calculated neutron diffraction patterns of $Fe_{1.8}Mn_{0.2}P_{0.9}Si_{0.1}$ in the antiferromagnetic state, for the model with moments along *b* axis (b) Refinement comparison of magnetic models with moments along the *c*-axis, *b*-axis, and within the *ab*-plane, shown for the enlarged magnetic satellite peaks. Dashed lines represent the magnetic contribution of each model, while the total calculated intensity for the model with moments along the *b*-axis is shown in as a green line. The HKL indices of the main Bragg reflections and their corresponding magnetic satellites are indicated.

Liu: Data curation, Formal analysis, Investigation, Writing - review and editing **Lennart Häggström**: Conceptualization, Data curation, Formal analysis, Investigation, Methodology, Visualization, Writing - original draft, Writing - review and editing **Fredrik Lindgren**: Data curation, Investigation, Methodology, Writing - review and editing **Vladimir Pomjakushin**: Data curation, Investigation, Writing - review and editing **Premysl Beran**: Data curation, Formal analysis, Investigation, Methodology, Writing - review and editing **Oliver Gutfleisch**: Formal analysis, Writing - review and editing **Peter Svedlindh**: Data curation, Investigation, Methodology, Writing - review and editing **Johan Cedervall**: Conceptualization, Data curation, Formal analysis, Investigation, Methodology, Visualization, Writing - original draft, Writing - review and editing

Conflicts of interest

There are no conflicts to declare.

Data availability

The data that support the findings of this study are available from the corresponding author upon reasonable request. Researchers interested in accessing these datasets for replication or further studies can contact the corresponding author to request the necessary materials.

Acknowledgements

Financial support from the ÅForsk Foundation (grant nr. 22-378), the Swedish Foundation for Strategic Research (SSF) through SwedNess (grant nr. GS1715-0008) and WISE - Wallenberg Initiative Materials Science for Sustainability is gratefully acknowledged. This work is based on experiments performed at the Swiss spallation neutron source SINQ, Paul Scherrer Institute, Villigen, Switzerland.

Notes and references

1 E. Brück, *Journal of Physics D: Applied Physics*, 2005, **38**, R381.
2 V. V. Khovaylo, V. V. Rodionova, S. N. Shevyrtalov and V. Novosad, *Physica Status Solidi (B) Basic Research*, 2014, **251**, 2104–2113.
3 E. L. França, A. O. D. Santos, A. A. Coelho and L. M. D. Silva, *Journal of Magnetism and Magnetic Materials*, 2016, **401**, 1088–1092.
4 K. A. Gschneidner and V. K. Pecharsky, *International Journal of Refrigeration*, 2008, **31**, 945–961.
5 N. H. Dung, Z. Q. Ou, L. Caron, L. Zhang, D. T. Thanh, G. A. D. Wijs, R. A. D. Groot, K. H. Buschow and E. Brück, *Advanced Energy Materials*, 2011, **1**, 1215–1219.
6 H. Yibole, F. Guillou, L. Zhang, N. H. V. Dijk and E. Brück, *Journal of Physics D: Applied Physics*, 2014, **47**, 075002.
7 L. Lundgren, G. Tarmohamed, O. Beckman, B. Carlsson and S. Rundqvist, *Physica Scripta*, 1978, **17**, 39.
8 N. T. Trung, Z. Q. Ou, T. J. Gortenmulder, O. Tegus, K. H. Buschow and E. Brück, *Applied Physics Letters*, 2009, **94**, 102513.
9 F. Guillou, G. Porcari, H. Yibole, N. V. Dijk and E. Brück, *Advanced Materials*, 2014, **26**, 2671–2675.
10 D. T. C. Thanh, E. Brück, N. T. Trung, J. C. Klaasse, K. H. Buschow, Z. Q. Ou, O. Tegus and L. Caron, *Journal of Applied Physics*, 2008, **103**, 07B318.
11 M. Bacmann, J.-L. Soubeyroux, R. Barrett, D. Fruchart,

View Article Online
DOI: 10.1039/D5TA03047A

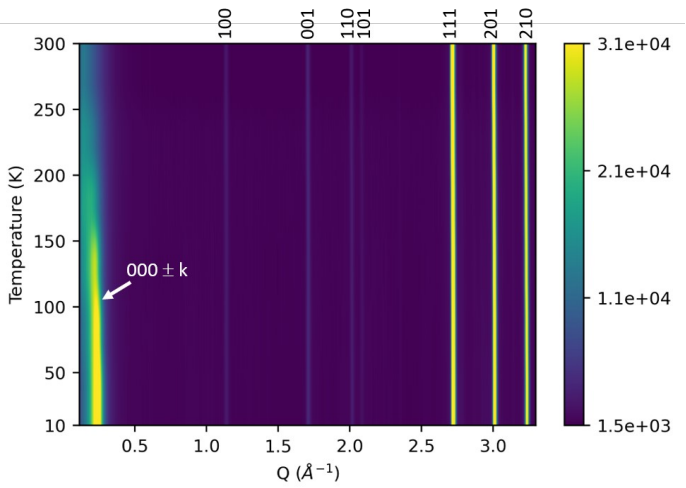

Fig. 11 Heat map of the evolution of the diffraction data for x = 0.1 sample in the Q region 0 to 3.3 Å^{-1} on cooling. The pure magnetic reflection 000 ± k (k = (0.2203 0 0)) has an increase in intensity below ≈ 150 K and shows broadening compared to the nuclear Bragg peaks in the figure.

R. Zach, S. N. ' and R. Fruchart, *Journal of Magnetism and Magnetic Materials*, 1994, **134**, 59–67.

12 M. Hudl, P. Nordblad, T. Björkman, O. Eriksson, L. Häggström, M. Sahlberg, Y. Andersson, E. K. Delczeg-Czirjak and L. Vitos, *Physical Review B - Condensed Matter and Materials Physics*, 2011, **83**, 134420.

13 N. H. Dung, L. Zhang, Z. Q. Ou, L. Zhao, L. V. Eijck, A. M. Mulders, M. Avdeev, E. Suard, N. H. V. Dijk and E. Brück, *Physical Review B - Condensed Matter and Materials Physics*, 2012, **86**, 045134.

14 B. Malaman, G. L. Caër, P. Delcroix, D. Fruchart, M. Bacmann and R. Fruchart, *Journal of Physics: Condensed Matter*, 1996, **8**, 8653.

15 D. Fruchart, S. Haj-Khlifa, P. de Rango, M. Balli, R. Zach, W. Chajec, P. Fornal, J. Stanek, S. Kaprzyk and J. Tobola, *Crystals*, 2019, **9**, 37.

16 X. F. Miao, L. Caron, P. Roy, N. H. Dung, L. Zhang, W. A. Kockelmann, R. A. de Groot, N. H. van Dijk and E. Brück, *Phys. Rev. B*, 2014, **89**, 174429.

17 P. Jernberg, A. Yousif, L. Häggström and Y. Andersson, *Journal of Solid State Chemistry*, 1984, **53**, 313–322.

18 R. Wäppling, L. Häggström, T. Ericsson, S. Devanarayanan, E. Karlsson, B. Carlsson and S. Rundqvist, *Journal of Solid State Chemistry*, 1975, **13**, 258–271.

19 S. Ghorai, J. Cedervall, R. Clulow, S. Huang, T. Ericsson, L. Häggström, V. Shtender, E. K. Delczeg-Czirjak, L. Vitos, O. Eriksson, M. Sahlberg and P. Svedlindh, *Phys. Rev. B*, 2023, **107**, 104409.

20 T. Gottschall, K. P. Skokov, M. Fries, A. Taubel, I. Radulov, F. Scheibel, D. Benke, S. Riegg and O. Gutfleisch, *Advanced Energy Materials*, 2019, **9**, 1901322.

21 V. Höglin, M. Hudl, L. Caron, P. Beran, M. H. Sørby, P. Nordblad, Y. Andersson and M. Sahlberg, *Journal of Solid State Chemistry*, 2015, **221**, 240–246.

22 V. Höglin, M. Hudl, M. Sahlberg, P. Nordblad, P. Beran and Y. Andersson, *Journal of Solid State Chemistry*, 2011, **184**, 2434–2438.

23 K. Katagiri, K. Nakamura and H. Wada, *Journal of Alloys and Compounds*, 2013, **553**, 286–290.

24 B. Carlsson, M. Gölin and S. Rundqvist, *Journal of Solid State Chemistry*, 1973, **8**, 57 – 67.

25 P. Fischer, G. Frey, M. Koch, M. Könnecke, V. Pomjakushin, J. Schefer, R. Thut, N. Schlumpf, R. Bürge, U. Greuter, S. Bondt and E. Berruyer, *Physica B: Condensed Matter*, 2000, **276-278**, 146–147.

26 H. M. Rietveld, *Journal of Applied Crystallography*, 1969, **2**, 65–71.

27 J. Rodriguez-Carvajal, *Physica B: Condensed Matter*, 1993, **192**, 55 – 69.

28 A. Wills, *Physica B: Condensed Matter*, 2000, **276-278**, 680–681.

29 M. J. Neish, M. P. Oxley, J. Guo, B. C. Sales, L. J. Allen and M. F. Chisholm, *Phys. Rev. Lett.*, 2015, **114**, 106101.

30 J. Cedervall, M. S. Andersson, E. K. Delczeg-Czirjak, D. Iuşan, M. Pereiro, P. Roy, T. Ericsson, L. Häggström, W. Lohstroh, H. Mutka, M. Sahlberg, P. Nordblad and P. P. Deen, *Phys. Rev. B*, 2019, **99**, 174437.

31 T. Ericsson, L. Häggström, R. Wäppling and T. Methasiri, *Physica scripta*, 1980, **21**, 212.

32 S. Mugiraneza and A. M. Hallas, *Communications Physics*, 2022, **5**, 95.

33 S. Ghorai, V. Shtender, P. Ström, R. Skini and P. Svedlindh, *Journal of Alloys and Compounds*, 2022, **895**, 162714.

34 S. Ghorai, S. A. Ivanov, R. Skini and P. Svedlindh, *Journal of Physics: Condensed Matter*, 2021, **33**, 145801.

35 Z. Q. Ou, L. Zhang, N. H. Dung, L. V. Eijck, A. M. Mulders, M. Avdeev, N. H. V. Dijk and E. Brück, *Journal of Magnetism and Magnetic Materials*, 2013, **340**, 80–85.

36 X.-F. Miao, S.-Y. Hu, F. Xu and E. Brück, *Rare Metals*, 2018, **37**, 723–733.

37 X. Miao, L. Caron, J. Cedervall, P. Gubbens, P. Dalmas de

View Article Online
DOI: 10.1039/D5TA03047A

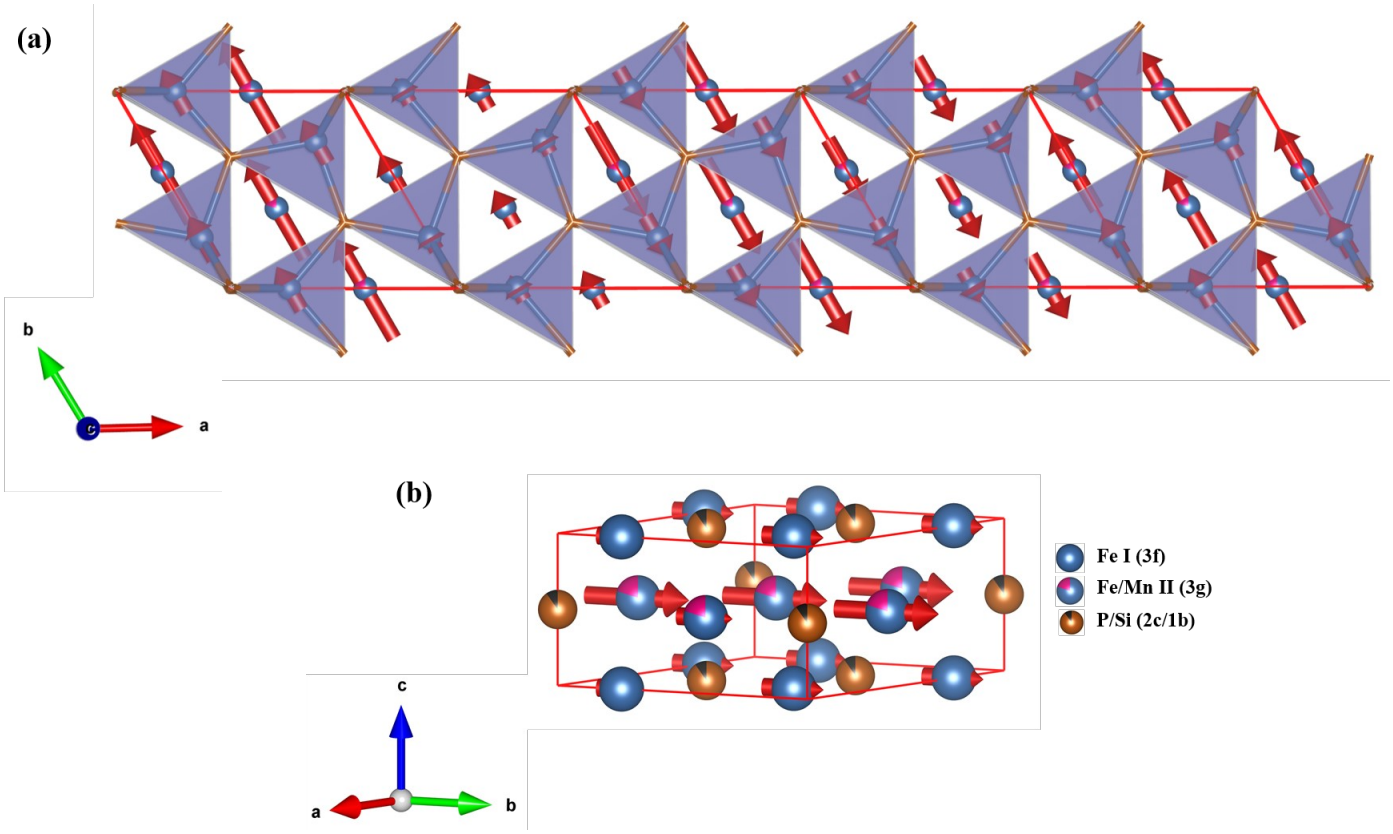

Fig. 12 (a) Magnetic structure depicting the propagation of magnetic moments along a-axis. Fe I atoms sitting at the $3f$ site are shown inside polyhedra (c) Unit cell with magnetic moments pointing along the b-axis.

Réotier, A. Yaouanc, F. Qian, A. Wildes, H. Luetkens, A. Amato *et al.*, *Physical Review B*, 2016, **94**, 014426.

38 A. Singh, S. Mohapatra, P. Khare, N. Ganguli, A. Wildes, V. Siruguri and S. Kaushik, *Materials Research Express*, 2019, **6**, 066107.

39 G. Li, W. Li, S. Schönecker, X. Li, E. K. Delczeg-Czirjak, Y. O. Kvashnin, O. Eriksson, B. Johansson and L. Vitos, *Applied Physics Letters*, 2014, **105**, 262405.

View Article Online
DOI: 10.1039/D5TA03047A

Data Availability Statement

The data that support the findings of this study are available from the corresponding author upon reasonable request. Researchers interested in accessing these datasets for replication or further studies can contact the corresponding author to request the necessary materials.